GMR
The Original

OXYSTELMA ESCULENTUM-MEDIATED AG/AGCL NANOPARTICLES AS POTENT ANTINEOPLASTIC AGENTS AGAINST MCF-7, HELA, AND HEPG2 CELLS: DLS-GUIDED SYNTHESIS, MULTI-TECHNIQUE CHARACTERIZATION, AND ANTIOXIDANT PROFILING

Muhammad Akhlaq[1,2*], Maria Manan[3], Shafqat Rasool[4], Aneeba Arshad[5], Ahsan Ali[6], Hina Mumtaz[7], Ramla Shabbir[8], Asma Yawar[9], Shiv Ram Ashraf [10], Hafiz Abdul Sattar Hashmi[11]**

[1]Office of Research, Innovation and Commercialization (ORIC), Hamdard University, Karachi, Pakistan
[2]The Islamia University of Bahawalpur, Bahawalpur, Pakistan
[3]Department of Pharmaceutical Chemistry, Faculty of Pharmaceutical Sciences, Government College University Faisalabad, Pakistan (mariamanan43@yahoo.com)
[4]School of Eastern Medicine, Minhaj University Lahore, Pakistan (Orcid ID 0009-0001-0115-3530) shafqatrasool.em@mul.edu.pk
[5]Faculty of Pharmacy, The Superior University, Main Campus, Lahore, Pakistan (Email aneebaarshad44@gmail.com ORCID: 0009-0006-3317-309X)
[6]College of Pharmacy, Lyallpur Institute of Advanced Studies, Faisalabad, Pakistan (drahsanalishiekh@gmail.com; ORCID: 0000-0003-4346-0667)
[7]Faculty of Pharmaceutical Sciences, Government College University Faisalabad, Pakistan (mumtazhina32@gmail.com)
[8]Faculty of Pharmacy, The University of Lahore, Pakistan (ramla.kashif@pharm.uol.edu.pk)
[9]Department of Nutritional Sciences, Faculty of Science and Technology, Government College Women University Faisalabad, Pakistan (Asmabukhari758@gmail.com)
[10]Department of Biochemistry and Biotechnology, University of Gujrat, Pakistan (shivramashraf@yahoo.com; ORCID: 0000-0002-1082-843X)
[11]University College of Conventional Medicine, Faculty of Medicine &Allied Health Sciences, The Islamia University of Bahawalpur, Pakistan (sattarhashmi5767@gmail.com; abdul.sattar@iub.edu.pk; https://orcid.org/0000-0002-6898-6852)
***Corresponding author:** *Muhammad Akhlaq. Email: muhammadakhlaq377@gmail.com*
**** Corresponding author:** *Hafiz Abdul Sattar Hashmi (sattarhashmi5767@gmail.com; abdul.sattar@iub.edu.pk;*

ABSTRACT

Background: Plant-mediated (green) synthesis of silver nanoparticles (Ag-NPs) offers an eco-friendly alternative to physicochemical synthesis routes and is increasingly explored as a source of anticancer and antioxidant nanomedicine agents.

Objectives: To establish the in vitro antineoplastic potential of Oxystelma esculentum-mediated Ag/AgCl nanoparticles against three human cancer cell lines, underpinned by DLS-guided formulation optimization, comprehensive physicochemical characterization, and antioxidant profiling.

Methods: Five Ag-NP formulations (F1–F5) were synthesized at increasing plant-extract concentration and screened by DLS particle sizing; the optimum formulation was additionally characterized by zeta potential, UV-Visible spectroscopy, powder X-ray diffraction (XRD; Scherrer and Williamson–Hall analysis), scanning electron microscopy (SEM) with automated particle-size-distribution analysis, energy-dispersive X-ray spectroscopy (EDX; four independent spectra), and Fourier-transform infrared (FTIR) spectroscopy. Antineoplastic activity was assessed by MTT assay against MCF-7, HeLa, and HepG2 cell lines in three independent biological replicates (n = 3), analysed by two-way ANOVA with Tukey's post hoc test, and antioxidant activity by the DPPH radical-scavenging assay (n = 3), with one-way ANOVA applied to the DPPH dataset.

Results: DLS screening showed particle size increasing monotonically with extract concentration (92–113 nm across F1–F5); the lowest-extract formulation (F1, 92 nm) was selected as optimum and carried forward for full characterization, with a zeta potential of −24.8 mV indicating moderate colloidal stability. UV-Vis analysis of the optimum formulation showed a surface plasmon resonance band at 430 nm. XRD confirmed a biphasic crystalline product comprising metallic Ag^0 and AgCl, with Scherrer crystallite sizes of 27.6 ± 8.4 nm and 29.4 ± 3.9 nm, respectively. SEM revealed quasi-spherical particles (pooled mean diameter 74.3 ± 56.7 nm, n = 2,203; primary-particle estimate 50.7 ± 37.7 nm at highest resolution), and EDX (mean of four spectra) confirmed Ag (10.90 ± 0.51 wt%) alongside Cl (5.38 ± 0.42 wt%; Ag:Cl atomic ratio 0.67 ± 0.02) and a C/N/O-rich organic capping layer, consistent with FTIR-identified O–H/N–H, C=C/amide, C–N/carboxylate, and Ag–O vibrations. Ag/AgCl NPs showed concentration-dependent cytotoxicity against MCF-7, HeLa, and HepG2 cells with mean IC50 values of 1.10 ± 0.04, 0.90 ± 0.03, and 0.90 ± 0.03 µg/mL (mean ± SD, n = 3), respectively, with significant concentration, cell-line, and interaction effects (two-way ANOVA, all $p < 0.0001$) — substantially more potent than several recently reported plant-mediated Ag-NP systems. DPPH scavenging increased significantly with concentration (one-way ANOVA, $F(4,10) = 399.0$, $p < 0.0001$), with an IC50 of 83.63 ± 1.37 µg/mL.

Conclusion: Oxystelma esculentum-mediated Ag/AgCl nanoparticles, produced via a DLS-guided formulation-optimization strategy, combine well-defined physicochemical properties and moderate colloidal stability with substantial anticancer potency and moderate antioxidant activity, supporting their candidacy for further pharmacological investigation as antineoplastic agents.

KEYWORDS: *Green synthesis; Silver nanoparticles; Ag/AgCl; Oxystelma esculentum; Dynamic light scattering; Antineoplastic agents; Antioxidants*

INTRODUCTION

Nanotechnology has emerged as a transformative field in biomedicine, with metallic nanoparticles occupying a central role owing to their unique size-dependent optical, electronic, and biological properties (Khan et al., 2019; Maqbool et al., 2026). Among these, silver nanoparticles (Ag-NPs) are among the most extensively studied nanomaterials for antimicrobial, antioxidant, and anticancer applications, owing to their high surface-to-volume ratio, tunable surface chemistry, and demonstrated ability to induce reactive-oxygen-species (ROS)-mediated apoptosis in cancer cells (Zhang et al., 2016).

Conventional physical and chemical methods of Ag-NP synthesis often involve toxic reducing agents, high energy input, and generate hazardous by-products, limiting their biomedical applicability. Green (plant-mediated) synthesis has therefore gained prominence as a low-cost, eco-friendly alternative in which phytochemicals — polyphenols, flavonoids, and proteins present in plant extracts — simultaneously act as reducing and capping agents, yielding biocompatible nanoparticles without the need for hazardous chemicals (Ahmed et al., 2016; Zhang et al., 2016). A growing body of literature has demonstrated that plant-mediated Ag-NPs frequently exhibit potent, selective cytotoxicity toward cancer cell lines at low microgram concentrations, in some cases approaching the potency of established chemotherapeutics (Zhang et al., 2016; Ullah et al., 2020).

A frequently under-addressed step in green nanoparticle synthesis is formulation optimization: the extract-to-precursor ratio strongly influences particle size, size distribution, and colloidal stability, yet many studies characterize only a single, arbitrarily chosen formulation. Dynamic light scattering (DLS) provides a rapid, solution-phase screening tool for hydrodynamic particle size across a formulation series, allowing an evidence-based selection of the optimum batch prior to committing to the more resource-intensive suite of structural and elemental characterization techniques (electron microscopy, diffraction, and spectroscopy). Complementing DLS with zeta-potential measurement further allows the electrostatic contribution to colloidal stability to be quantified directly (Bhattacharjee, 2016).

Despite the extensive literature on plant-mediated Ag-NPs, relatively few studies combine a DLS-guided formulation-optimization step with a rigorous, multi-technique physicochemical characterization (optical, crystallographic, morphological, elemental, and vibrational) and a quantitative, multi-cell-line evaluation of anticancer potency and antioxidant capacity for the same optimized nanoparticle batch. Furthermore, an often under-reported but mechanistically important feature of green-synthesized Ag-NPs is the frequent co-formation of silver chloride (AgCl) alongside metallic Ag^0, arising from residual chloride ions in plant extracts — a biphasic Ag^0/AgCl system that is itself of interest for plasmonic photocatalysis (Lin et al., 2015), yet is rarely characterized or reported explicitly in the green-synthesis anticancer literature.

Oxystelma esculentum (family Apocynaceae, subfamily Asclepiadoideae) is a medicinal climbing plant traditionally used for its phytochemical-rich latex and leaf extracts (reported to contain pregnane glycosides, cardenolides, and flavonoids), but its potential as a reducing/capping agent for nanoparticle biosynthesis remains largely unexplored.

Given this gap, the central objective of the present study was to establish the in vitro antineoplastic potential of Oxystelma esculentum-mediated Ag-NPs against three human cancer cell lines (MCF-7, HeLa, and HepG2), relative to a taxol positive control and benchmarked against recently published plant-mediated Ag-NP systems evaluated against comparable cell lines. This was pursued by (i) biosynthesizing Ag-NPs using an extract of Oxystelma esculentum across a concentration series of five formulations; (ii) identifying the optimum formulation by DLS-based particle-size screening; (iii) comprehensively characterizing the optimum nanomaterial using zeta potential, UV-Vis spectroscopy, XRD, SEM, EDX, and FTIR, so that the structural basis of any observed anticancer activity could be identified; and (iv) evaluating antineoplastic activity by MTT assay, alongside antioxidant capacity by the DPPH radical-scavenging assay as a secondary readout. A specific hypothesis tested was that the nanoparticles' physicochemical identity (crystalline phase composition, particle size, and surface chemistry) could be coherently related to their observed antineoplastic activity.

MATERIALS AND METHODS

Chemicals and reagents

Silver nitrate ($AgNO_3$, >99.9% purity, Sigma-Aldrich, USA) and all other chemicals used were of analytical grade. MCF-7 (breast), HeLa (cervical), and HepG2 (liver) human cancer cell lines were obtained from the American Type Culture Collection (ATCC, Manassas, VA, USA). 2,2-Diphenyl-1-picrylhydrazyl (DPPH), 3-(4,5-dimethylthiazol-2-yl)-2,5-diphenyltetrazolium bromide (MTT), and taxol (positive control) were procured from Sigma-Aldrich (St. Louis, MO, USA). Cell culture media (Dulbecco's Modified Eagle Medium, DMEM), fetal bovine serum, and antibiotics (penicillin–streptomycin) were obtained from Sigma-Aldrich (St. Louis, MO, USA).

Plant material and extract preparation

Fresh leaves of Oxystelma esculentum were collected from the bank of the Shashmahi canal, Bahawalpur, Punjab, Pakistan, and authenticated by Dr. Ghulam Sarwar (Department of Botany, The Islamia University of Bahawalpur; voucher specimen no. Ref. Botany/160). The leaves were washed thoroughly with distilled water and shade-dried at room temperature. The dried material was coarsely powdered, and 100 g of leaf powder was subjected to cold

maceration in 500 mL of 100% ethanol for 48 h under continuous magnetic stirring at room temperature (repeated three times). The extract was filtered (Whatman No. 1), concentrated under reduced pressure at 35 °C using a rotary evaporator, and stored at 4 °C until further use.

Green synthesis of Ag/AgCl nanoparticles and DLS-guided formulation screening

Aqueous $AgNO_3$ solution (1 mM) was prepared, and the O. esculentum extract was added to 100 mL of the 1 mM $AgNO_3$ solution at five increasing extract-to-$AgNO_3$ volume ratios (ranging from 1:9 to 1:1), yielding five formulations (F1–F5, in order of increasing extract concentration) under continuous magnetic stirring. The reaction was carried out at 60 °C for 2 h, during which a visible colour change from pale yellow to dark brown indicated nanoparticle formation. Each suspension was centrifuged at 12,000 rpm for 20 min, and the pellet was washed three times with distilled water and ethanol to remove unreacted precursor and unbound phytochemicals, then dried in a vacuum oven at 60 °C overnight to obtain the Ag-NP powder.

All five formulations were first screened by dynamic light scattering (DLS) to determine average hydrodynamic particle size (Section 2.4). The formulation giving the smallest, most homogeneous particle size (F1) was selected as the optimum batch and carried forward for zeta-potential measurement and the full physicochemical (UV-Vis, XRD, SEM, EDX, FTIR) and biological (MTT, DPPH) characterization reported in this manuscript.

Physicochemical characterization

UV-Visible absorption spectra (200–800 nm) of the colloidal Ag-NP suspension (optimum formulation) were recorded on a UV-Vis spectrophotometer (Shimadzu UV-1800, Tokyo, Japan) to confirm surface plasmon resonance; readings below 290 nm were affected by detector overflow (saturation) due to the high optical density of the concentrated colloid and were excluded from analysis.

Powder XRD data were collected over $2\theta = 10–90°$ (Cu-Kα, $\lambda = 1.5406$ Å, step size 0.02°) on an X-ray diffractometer (PANalytical X'Pert POWDER, Malvern PANalytical, Netherlands); each reflection was fitted with a Gaussian profile on a linear background to extract peak position and full width at half maximum (FWHM), and peaks were indexed against JCPDS reference cards 31-1238 (AgCl) and 04-0783 (Ag^0). Average crystallite size was calculated using the Scherrer equation, $D = K\lambda/(\beta \cos\theta)$ ($K = 0.9$) (Scherrer, 1918), with a complementary Williamson–Hall analysis, $\beta \cos\theta = (K\lambda/D) + 4\varepsilon \sin\theta$ (Williamson and Hall, 1953), used to separate crystallite-size and microstrain contributions for each phase. Instrumental line broadening was not independently deconvoluted (no reference standard such as Si or LaB_6 was available), so reported Scherrer sizes represent upper-bound estimates of the true crystallite size.

Surface morphology was examined by scanning electron microscopy (JEOL JSM-5910, 15 kV accelerating voltage, 8 mm working distance, secondary-electron imaging mode) across a magnification series from 1,000× to 30,000×. Particle-size distributions were extracted from the three highest-magnification micrographs using automated background-flattened Otsu thresholding and connected-component segmentation (Python, scikit-image/OpenCV): the instrument scale bar was measured in pixels and converted to a nm/pixel calibration factor for each magnification (10.00 nm/px for the two 10,000× fields; 3.29 nm/px for the 30,000× field), uneven background shading was removed by large-kernel Gaussian background subtraction, particles were segmented by Otsu thresholding, and the equivalent circular diameter ($ECD = \sqrt{(4 \times Area/\pi)}$) was computed for every retained particle (3–300 nm size filter). Elemental composition was determined by EDX coupled to the SEM at four independent points/spectra on the sample, using the normalized, iterative (4–5-cycle) processing method with no peaks omitted, allowing the mean elemental composition to be reported with an associated standard deviation.

FTIR spectra (4000–600 cm^{-1}, 4 cm^{-1} resolution, 16 co-added scans) were recorded on a Bruker Alpha-P FTIR spectrometer (Bruker Optics, Germany; ZnSe beamsplitter, RT-DLaTGS detector) in four replicate scans were acquired, and the atmosphere-corrected, instrument-processed spectrum (showing the least deviation from the four-scan consensus average) was used for band assignment.

Dynamic light scattering and zeta potential

Hydrodynamic particle size of all five formulations (F1–F5) was measured by dynamic light scattering; zeta potential of the optimum formulation (F1) was measured by electrophoretic light scattering on a Malvern Zetasizer Nano ZS90 (Malvern Instruments, UK). Colloidal stability was classified against the conventional zeta-potential stability scale, in which a magnitude of 20–30 mV is considered to confer moderate electrostatic stabilization against aggregation, and values beyond ±30 mV are considered good-to-excellent (Bhattacharjee, 2016).

In vitro antineoplastic activity (MTT assay)

The cytotoxic potential of the biosynthesized Ag/AgCl nanoparticles (optimum formulation) was evaluated against MCF-7, HeLa, and HepG2 cell lines using the MTT colorimetric assay (Mosmann, 1983) in three independent biological replicates ($n = 3$). Cells were seeded in 96-well plates at a density of 1×10^4 cells/well in DMEM supplemented with 10% FBS and 1% penicillin–streptomycin and allowed to adhere for 24 h at 37 °C in a humidified 5% CO_2 atmosphere, then treated with Ag-NPs at concentrations of 1.25, 2.5, 5, and 10 µg/mL for 24 h, alongside taxol as a positive control and untreated cells as the negative control. Following incubation, 20 µL of MTT solution (0.5 mg/mL) was added to each well and incubated for 4 h; formazan crystals were dissolved in 150 µL of DMSO and absorbance was measured at 570 nm using a microplate reader (Bio-Rad Laboratories, USA). Percentage cytotoxicity was calculated relative to the untreated control. Data are expressed as mean ± SD of three independent biological replicates ($n = 3$).

DPPH radical-scavenging (antioxidant) assay

Antioxidant activity was assessed using the DPPH free-radical scavenging assay (Blois, 1958). Briefly, 1 mL of Ag-NP solution at concentrations of 50, 100, 200, 300, and 400 µg/mL was mixed with 2 mL of 0.1 mM

methanolic DPPH solution and incubated in the dark for 30 min at room temperature. Absorbance was measured at 517 nm, and percentage inhibition was calculated relative to the DPPH control. The assay was performed in independent triplicate (n = 3), and IC50 was determined for each replicate before calculating the mean ± SD.

Statistical analysis

Data are expressed as mean ± SD where replicate measurements were available (MTT assay, n = 3 independent biological replicates; DPPH assay, n = 3 independent replicates; EDX, n = 4 independent spectra; SEM particle-size distributions, n = 2,203 particles pooled from three fields of view). For the DPPH dataset, a one-way analysis of variance (ANOVA) was used to test for a significant concentration-dependent effect, computed from the reported group means, standard deviations, and replicate count (n = 3 per concentration) using the standard summary-statistics ANOVA formulation (between-groups and within-groups sums of squares); $p < 0.05$ was considered statistically significant. All statistical computations and graphs were prepared in Python (SciPy/Matplotlib) using a GraphPad Prism-style layout (symbol-and-error-bar dose–response plots, boxed test statistics); GraphPad Prism itself was not the software used, and this is noted for transparency. For the MTT dataset, cytotoxicity (% inhibition) was analysed from the individual replicate values (n = 3 per group) by two-way ANOVA with cell line and nanoparticle concentration as the two factors (standard balanced-design sums-of-squares formulation), followed by Tukey's multiple-comparison post hoc test comparing each concentration with the lowest concentration (1.25 µg/mL) within each cell line; the taxol positive control is shown for reference and was not included in the ANOVA model. IC50 values are reported as mean ± SD (n = 3).

RESULTS

UV-Visible spectroscopy

UV-Vis absorption spectroscopy (200–800 nm) was performed on the colloidal Ag-NP suspension of the optimum (F1) formulation. Readings below 290 nm were affected by detector overflow (saturation) due to the high optical density of the concentrated colloid and were excluded from analysis.

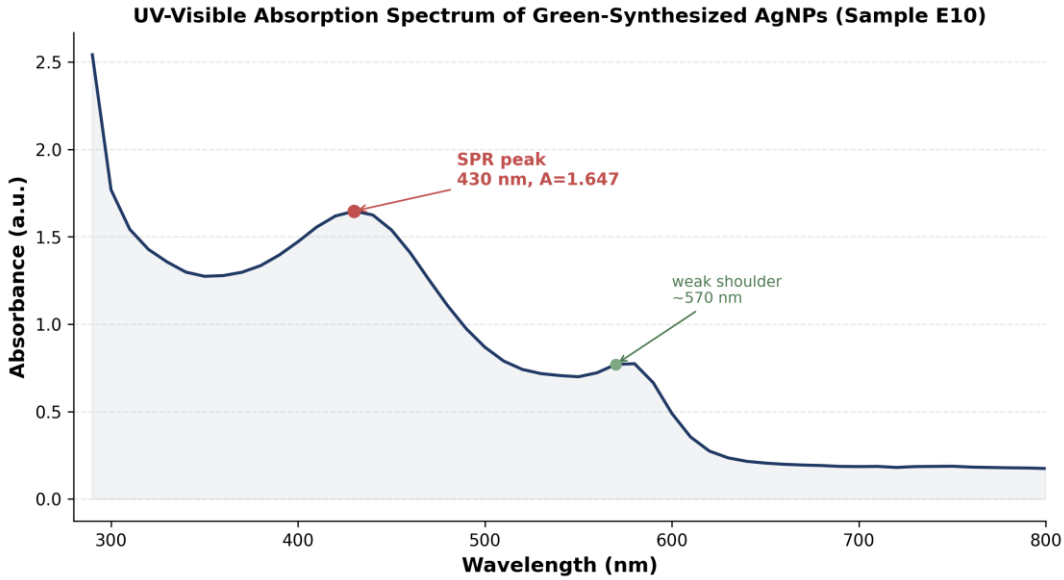


Fig. 1. UV-Visible absorption spectrum of the optimum-formulation Ag/AgCl nanoparticles, showing the surface plasmon resonance (SPR) band at 430 nm and a weak shoulder near 570–580 nm.

Spectral feature	Value	Significance
SPR peak position	430 nm	Typical of spherical, well-dispersed Ag-NPs
Peak absorbance	1.647 a.u.	Strong band; moderate–high yield
Band shape	Narrow, symmetric	Low polydispersity, largely spherical particles
Weak shoulder	~570–580 nm	Minor fraction of larger/aggregated particles
Baseline (650–800 nm)	0.17–0.19 a.u.	Flat, low tail — good colloidal stability

Table I. Key spectral features extracted from the UV-Vis spectrum.

The spectrum exhibited a well-defined absorption maximum at 430 nm with a narrow, symmetric band shape and a weak shoulder near 570–580 nm. The baseline beyond 650 nm remained low and flat (0.17–0.19 a.u.), consistent with a colloidally stable dispersion with minimal large-scale aggregation.

DLS-guided formulation screening and zeta potential

Average hydrodynamic particle size, measured by DLS, increased monotonically with increasing plant-extract concentration across the five synthesized formulations, from 92 nm (F1) to 113 nm (F5) (Table II, Fig. 2a),

consistent with extract-mediated agglomeration in which higher phytochemical/biomolecule loading promotes bridging and aggregation between nascent nanoparticles during reduction and capping.

Formulation	Plant-extract level	Avg. particle size (nm)	Zeta potential (mV)
F1 (optimum)	Lowest	92	−24.8
F2	Low–medium	98	—
F3	Medium	101	—
F4	Medium–high	105	—
F5	Highest	113	—

Table II. DLS-derived average particle size across the five formulations (F1–F5); zeta potential was measured only for the selected optimum formulation (F1).

Formulation F1 (lowest extract concentration) produced the smallest and most desirable particle size (92 nm) and was therefore selected as the optimum formulation for all subsequent physicochemical and biological characterization reported below.

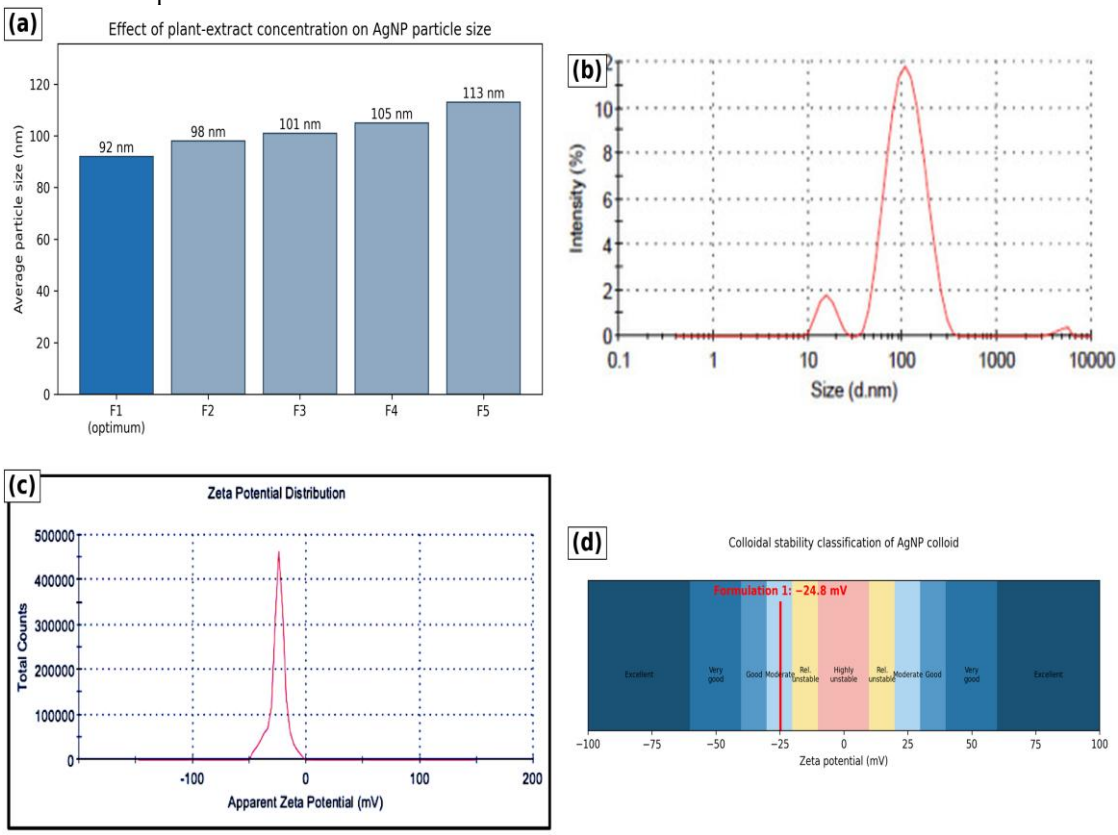


Fig. 2. DLS-guided formulation screening and zeta potential of the optimum Ag/AgCl nanoparticle formulation (F1). (a) Increase in average hydrodynamic size with increasing plant-extract concentration across formulations F1–F5. (b) DLS intensity-weighted particle-size distribution of F1. (c) Zeta potential distribution of F1, centred at −24.8 mV. (d) Classification of the measured zeta potential on the standard colloidal-stability scale.

The intensity-weighted size distribution of F1 (Fig. 2b) showed a dominant population centred at approximately 90–100 nm (peak intensity ≈ 11.5%), consistent with the reported average size of 92 nm, and a minor secondary population near 10–15 nm (peak intensity ≈ 1%). Because DLS intensity distributions are weighted by the sixth power of particle diameter, even a small number of larger aggregates can dominate the intensity signal; the distribution is therefore best interpreted as predominantly monomodal with a minor, low-intensity shoulder rather than a strongly bimodal population.

The zeta-potential distribution (Fig. 2c) showed a single, narrow, well-defined peak at −24.8 mV with no secondary populations, indicating a homogeneous surface charge across the particle population. On the conventional zeta-potential stability scale (Fig. 2d), this value falls within the moderate-stability range (20–30 mV magnitude) — sufficient for reasonable short-to-medium-term colloidal stability, aided further by steric stabilization from the adsorbed phytochemical capping layer typical of green-synthesized nanoparticles.

X-ray diffraction analysis

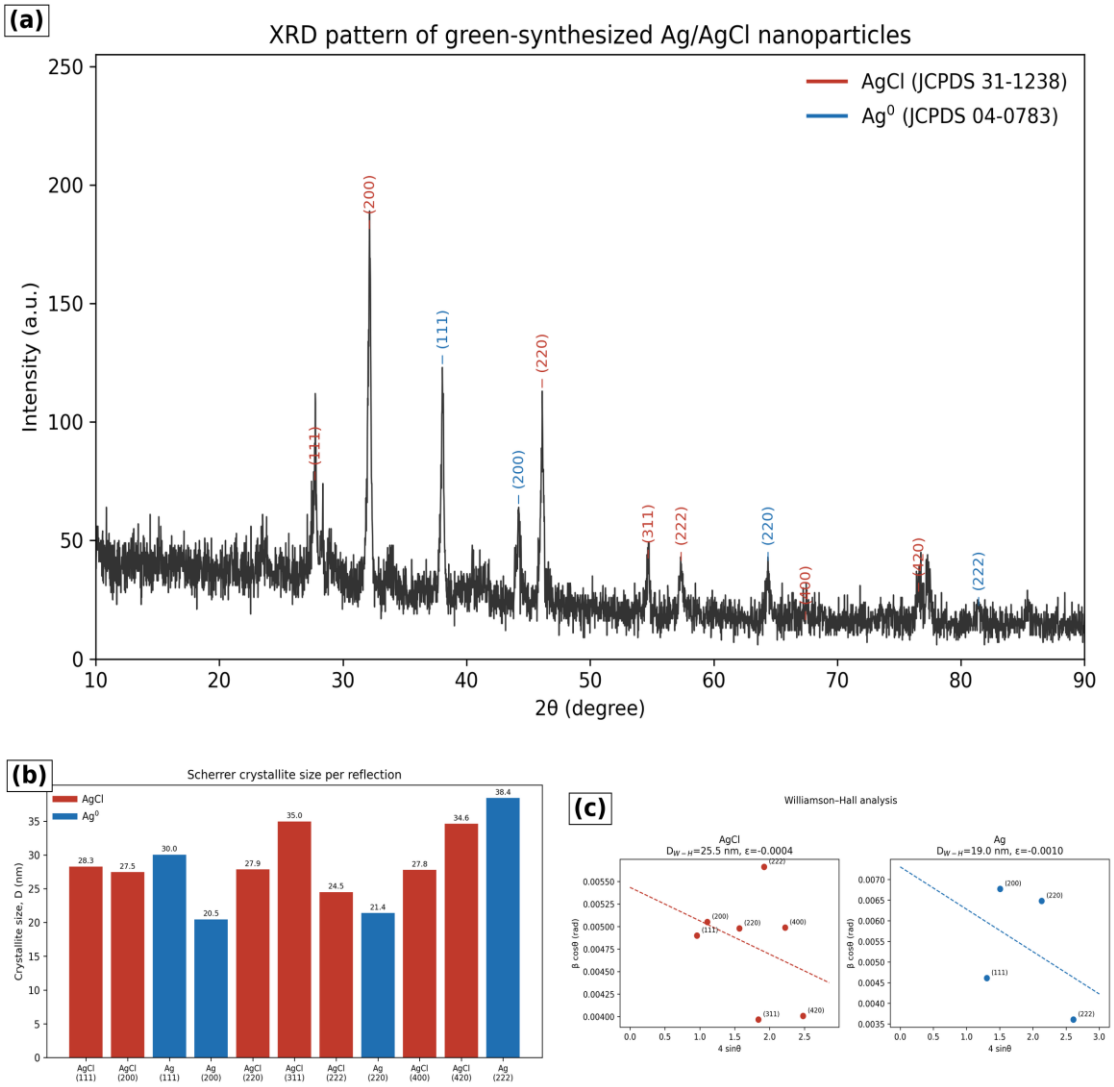


Fig. 3. X-ray diffraction analysis of the optimum-formulation Ag/AgCl nanoparticles. (a) Indexed powder XRD pattern; red markers: cubic AgCl (JCPDS 31-1238), blue markers: face-centred-cubic metallic Ag⁰ (JCPDS 04-0783). (b) Scherrer crystallite size calculated independently from each Bragg reflection, grouped by phase. (c) Williamson–Hall plots for the AgCl and Ag⁰ phases.

Eleven well-resolved Bragg reflections were indexed: seven to cubic AgCl (JCPDS 31-1238) and four to face-centred-cubic metallic Ag⁰ (JCPDS 04-0783). No reflections attributable to silver oxide or carbonate phases were observed, and the absence of a broad amorphous halo indicates a well-crystallized product.

2θ (°)	Phase	(hkl)	d (Å)	D Scherrer (nm)	a (Å)
27.74	AgCl	(111)	3.214	28.3	5.566
32.14	AgCl	(200)	2.782	27.5	5.565
38.05	Ag⁰	(111)	2.363	30.0	4.093
44.21	Ag⁰	(200)	2.047	20.5	4.094
46.12	AgCl	(220)	1.967	27.9	5.562
54.69	AgCl	(311)	1.677	35.0	5.562
57.36	AgCl	(222)	1.605	24.5	5.560
64.39	Ag⁰	(220)	1.446	21.4	4.089
67.43	AgCl	(400)	1.388	27.8	5.551
76.58	AgCl	(420)	1.243	34.6	5.560
81.43	Ag⁰	(222)	1.181	38.4	4.091

2θ (°)	Phase	(hkl)	d (Å)	D Scherrer (nm)	a (Å)
AgCl summary (7 peaks)	—	—	—	29.4 ± 3.9 (D W–H 25.5)	5.561 ± 0.005 (JCPDS 5.549)
Ag^0 summary (4 peaks)	—	—	—	27.6 ± 8.4 (D W–H 19.0)	4.092 ± 0.002 (JCPDS 4.086)

Table III. Indexed Bragg reflections with d-spacing, Scherrer crystallite size (D), and refined lattice parameter (a) for each peak, followed by per-phase summary rows (mean ± SD Scherrer size, Williamson–Hall size, and refined lattice parameter vs. JCPDS standard).

The refined lattice parameters (AgCl: 5.561 Å; Ag^0: 4.092 Å) matched the respective JCPDS standards within 0.2–0.3%, confirming correct phase assignment. Scherrer analysis (Fig. 3b) gave average crystallite sizes of 29.4 ± 3.9 nm (AgCl) and 27.6 ± 8.4 nm (Ag^0). Both phases showed a small negative Williamson–Hall slope (Fig. 3c), nominally indicating compressive lattice microstrain (ε = −0.0004 for AgCl, −0.0010 for Ag^0); given the limited number of reflections per phase (4–7), these strain values are reported as qualitative/supporting evidence, with the Scherrer average taken as the primary crystallite-size metric.

Morphological and elemental analysis (SEM/EDX)

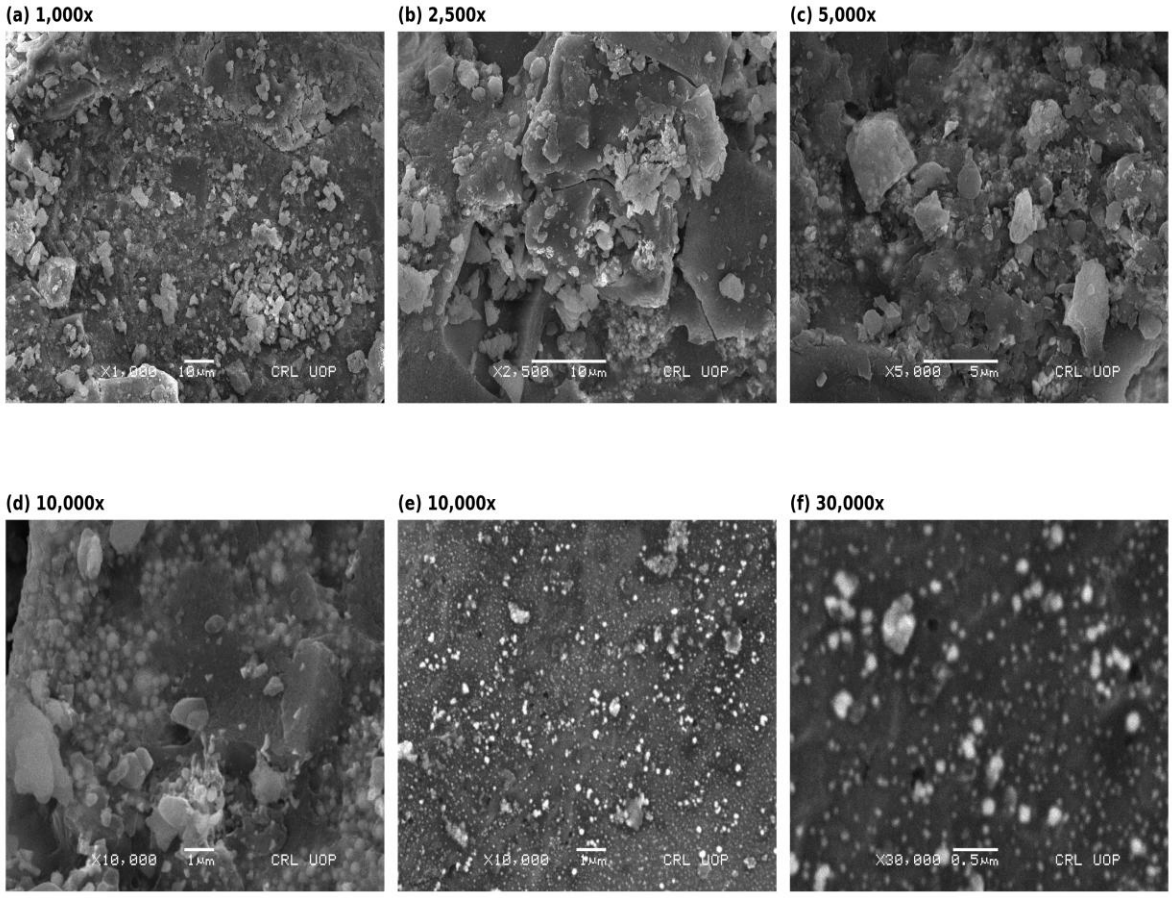


Fig. 4. SEM micrographs of the optimum Ag/AgCl nanoparticle formulation at increasing magnification: (a) 1,000×, (b) 2,500×, (c) 5,000×, (d) 10,000×, (e) 10,000× (second field of view), (f) 30,000×.

At low magnification (1,000–5,000×), an irregular, porous, micron-scale support/aggregate matrix was observed, with no individual nanoparticles resolvable. At 10,000× and above, a dense population of small, quasi-spherical, electron-bright particles was resolved, decorating the support surface as isolated particles and small agglomerates. Quantitative particle sizing performed on the three highest-magnification images (2,203 measured particles) is summarized in Table IV and Fig. 5.

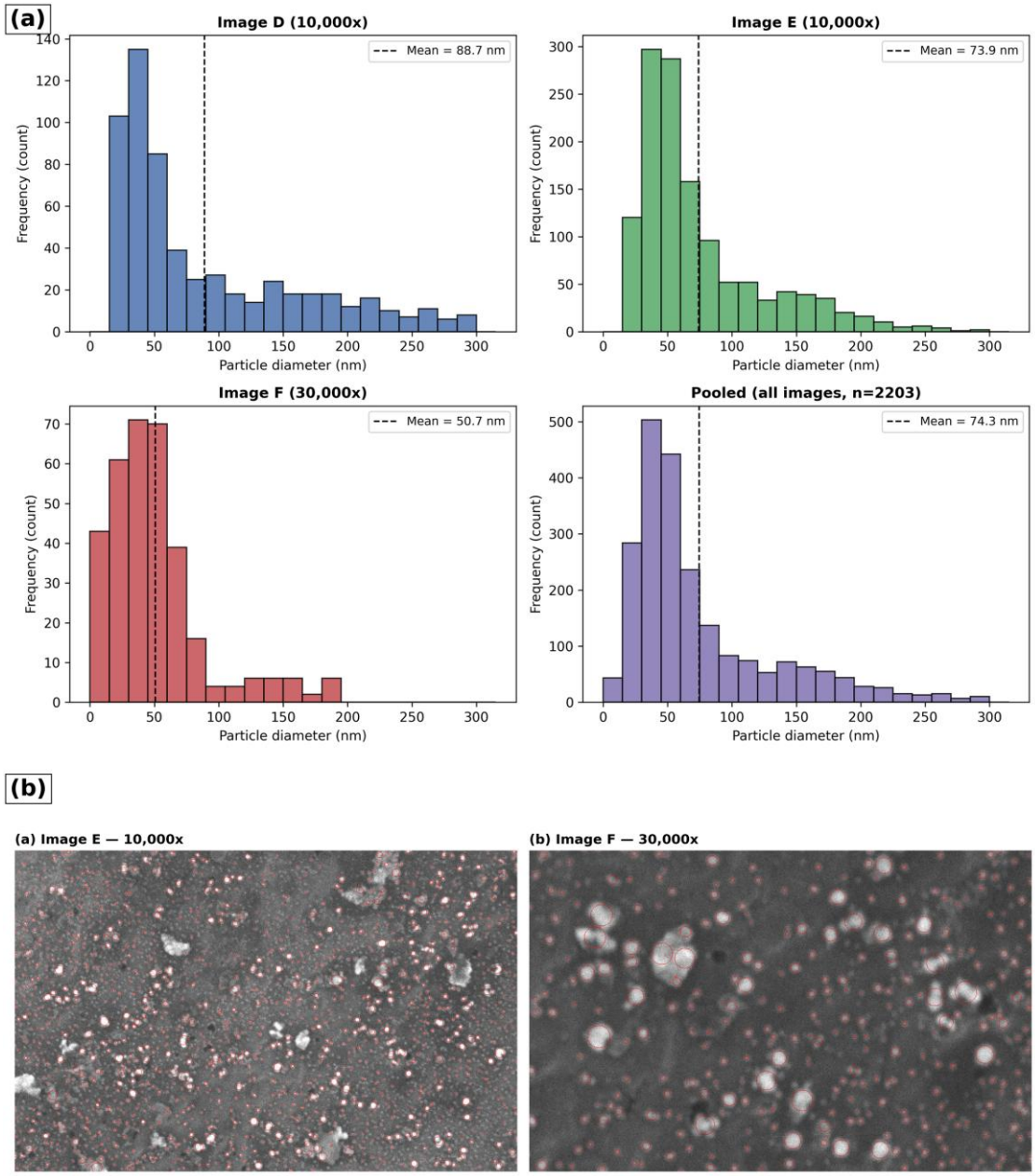


Fig. 5. Quantitative SEM particle-size analysis. (a) Particle-size-distribution histograms from images d, e, f, and pooled (n = 2,203); dashed lines mark the mean diameter. (b) Representative particle-detection overlays used for sizing, for the 10,000× (left) and 30,000× (right) fields of view.

Image	Magnification	N particles	Mean ± SD (nm)	Median (nm)	Range (nm)
d	10,000×	594	88.7 ± 72.6	55.8	25.2–298.8
e	10,000×	1275	73.9 ± 49.9	55.3	25.2–288.8
f	30,000×	334	50.7 ± 37.7	43.7	8.3–191.6
Pooled	—	2203	74.3 ± 56.7	52.9	8.3–298.8

Table IV. SEM-derived particle-size statistics.

The pooled mean particle diameter was 74.3 ± 56.7 nm (median 52.9 nm; coefficient of variation ≈ 76%), indicating a moderately polydisperse, right-skewed size distribution attributable to a minor fraction of agglomerated particles. Because the coarser pixel scale of the 10,000× images (10.0 nm/px) imposes a practical detection floor of ≈25 nm and biases their apparent means upward, the highest-resolution field (f, 30,000×, 3.29 nm/px) is considered the most reliable estimate of the primary particle size: 50.7 ± 37.7 nm (median 43.7 nm, range 8.3–191.6 nm).

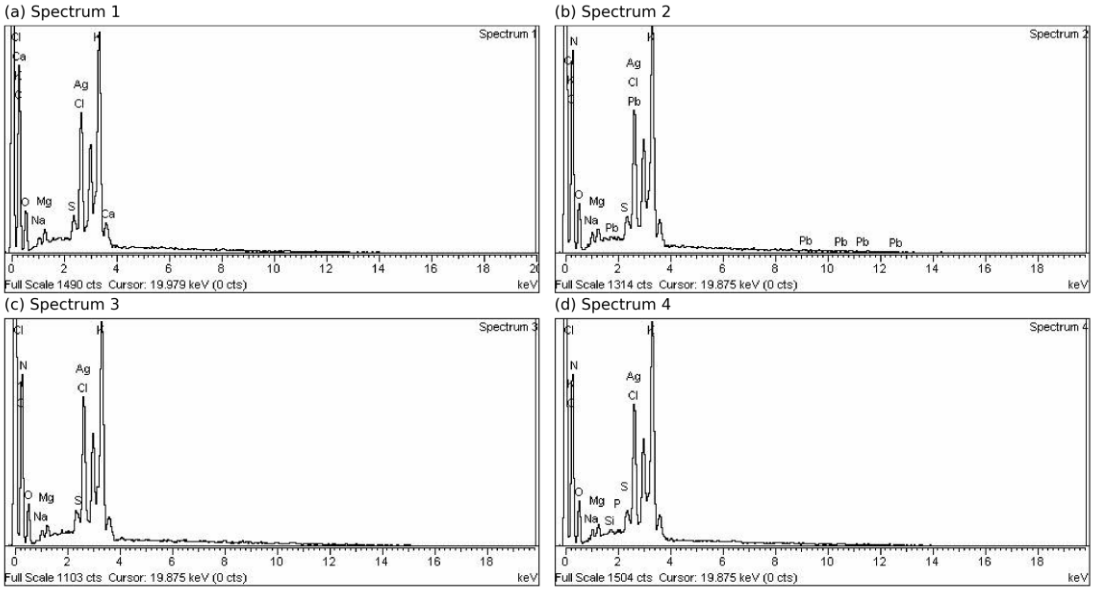


Fig. 6. EDX spectra acquired at four independent points on the Ag/AgCl nanoparticle sample.
Energy-dispersive X-ray spectroscopy was performed at four independent points/spots to verify elemental composition and its reproducibility across the specimen. All four spectra showed the same qualitative peak set — C, N, O, Na, Mg, S, Cl, K, and Ag were present in every spectrum, confirming homogeneous bulk composition. Two spectra additionally showed minor, spatially localized trace signals (Spectrum 1: Ca; Spectrum 2: Pb; Spectrum 4: Si, P), each appearing in only one of the four spectra and therefore attributed to point-specific surface contamination rather than a bulk constituent.

Element	Mean Weight (%)	SD (Wt%)	Mean Atomic (%)	SD (At%)	Assigned role
C K	46.10	5.06	63.12	6.48	Organic capping / phytochemical matrix
N K*	12.10	1.03	14.26	1.21	Proteins / amine-rich phytochemicals
O K	16.18	0.81	16.64	0.74	Hydroxyl/carbonyl groups, phenolics
Na K	0.60	0.06	0.42	0.05	Plant-extract residual salt
Mg K	0.54	0.05	0.37	0.03	Plant-extract residual mineral
S K	0.28	0.07	0.15	0.04	Sulfur-containing biomolecules
Cl K	5.38	0.42	2.50	0.19	AgCl phase (confirms XRD)
K K	10.29	0.58	4.33	0.24	Plant-extract residual salt
Ag L	10.90	0.51	1.66	0.08	Target nanoparticle element

Table V. Mean ± SD elemental composition (n = 4 spectra) with proposed assignment of each element's origin. *N was not detected in Spectrum 1 (Ca was present instead); the N mean/SD is therefore based on n = 3 spectra.

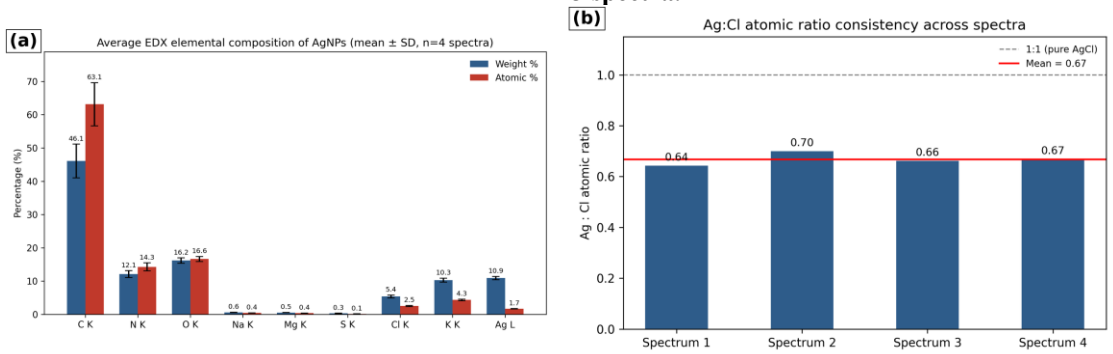


Fig. 7. EDX compositional summary. (a) Mean elemental composition (weight % and atomic %) averaged across the four spectra, error bars ± 1 SD. (b) Ag:Cl atomic ratio calculated independently from each of the four spectra, remaining consistent (0.64–0.70, mean 0.67 ± 0.02) and below the 1:1 stoichiometric line expected for pure AgCl.

For the nine elements detected in every spectrum, point-to-point variation was small relative to the mean, indicating good compositional homogeneity. The Ag content in particular was highly reproducible (10.19–11.37 wt% across individual spectra; coefficient of variation ≈ 4.7%), supporting a consistent nanoparticle yield across the sampled area.

The consistent co-occurrence of strong Ag and Cl signals at a stable Ag:Cl atomic ratio (Fig. 7b) provides direct compositional support for the biphasic Ag/AgCl system identified independently by XRD. An Ag:Cl ratio below unity in every spectrum indicates that not all silver is bound as AgCl — part of the Ag inventory exists as metallic Ag^0, in agreement with the XRD-based phase identification. The low spread in this ratio across four independently sampled points (SD = 0.02) indicates that the Ag/AgCl phase distribution is uniform throughout the sample rather than concentrated in isolated regions.

FTIR spectroscopy

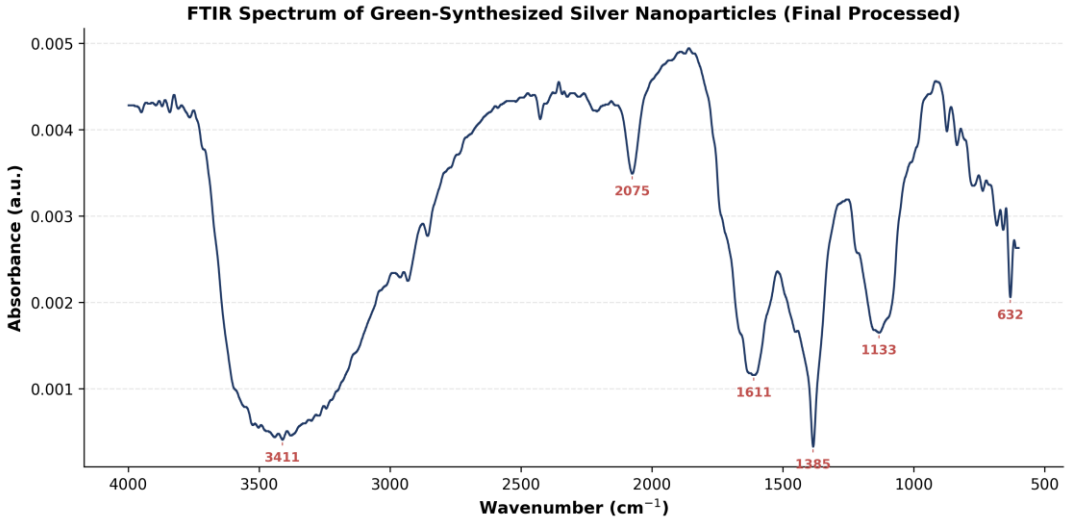


Fig. 8. Final, atmosphere-corrected FTIR spectrum of the optimum Ag/AgCl nanoparticle formulation, with major absorption bands labelled.

Wavenumber (cm^{-1})	Assignment	Likely origin
~3411 (broad, strong)	O–H / N–H stretching (H-bonded)	Phenolic/hydroxyl and amine groups from the reducing/capping agent
~2075 (weak)	Combination/overtone band	Low intensity; reported cautiously
~1611 (medium)	C=C aromatic / Amide I (C=O)	Polyphenolic ring or protein backbone
~1385 (strong, sharp)	C–N stretch / $–COO^-$ symmetric stretch	Aromatic amine or carboxylate groups
~1133 (medium)	C–O stretching	Ether/alcohol or polysaccharide C–O–C linkages
~632 (weak–medium)	Ag–O stretching vibration	Reported signature of Ag–O surface bonding

Table VI. Tentative assignment of the major FTIR absorption bands.

The FTIR spectrum showed no bands attributable to the metallic Ag core itself (Ag–Ag bonds are IR-inactive), but instead revealed a set of organic functional-group signatures consistent with a biomolecule-capped nanoparticle surface. The broad, strong band at ~3411 cm^{-1} indicates hydrogen-bonded O–H/N–H groups typical of phenolics, flavonoids, or proteins present in the reducing/stabilizing extract. The medium band near 1611 cm^{-1} (C=C aromatic/amide I) together with the strong, sharp band at ~1385 cm^{-1} (C–N or carboxylate stretching) points to aromatic ring systems and carboxylate/amine functionalities anchoring to the particle surface, a pattern widely reported for phytochemical-capped Ag-NPs. The band at ~1133 cm^{-1} (C–O stretching) further supports polyol/ether groups consistent with sugars or polyphenolic residues, while the weak band at ~632 cm^{-1}, frequently attributed in the literature to an Ag–O stretching vibration, offers indirect FTIR-level support for nanoparticle formation and surface functionalization, complementing the elemental Ag confirmation from EDX.

In vitro antineoplastic activity (MTT assay)

Ag/AgCl nanoparticles produced concentration-dependent cytotoxicity against all three cancer cell lines over the 1.25–10 µg/mL range in three independent biological replicates (Table VII, Fig. 9a,b). Against MCF-7 cells, cytotoxicity increased from 59.50 ± 1.30% (1.25 µg/mL) to 79.50 ± 1.30% (10 µg/mL; IC50 = 1.10 ± 0.04 µg/mL). Against HeLa cells, cytotoxicity increased from 71.70 ± 1.15% to 83.30 ± 1.15% (IC50 = 0.90 ± 0.03 µg/mL). Against HepG2 cells, cytotoxicity increased from 71.90 ± 1.15% to 83.50 ± 1.15% (IC50 = 0.90 ± 0.03 µg/mL).

The taxol positive control produced 89.20 ± 1.35%, 91.20 ± 1.31%, and 91.20 ± 1.31% inhibition in MCF-7, HeLa, and HepG2 cells, respectively, so that the highest nanoparticle concentration reached 89.1%, 91.3%, and 91.6% of the taxol response (mean values; all data mean ± SD, n = 3).

Concentration (µg/mL)	**MCF-7 % inhib. (R1, R2, R3)**	**MCF-7 % inhib. (mean ± SD)**	**HeLa % inhib. (R1, R2, R3)**	**HeLa % inhib. (mean ± SD)**	**HepG2 % inhib. (R1, R2, R3)**	**HepG2 % inhib. (mean ± SD)**
1.25	58.2, 60.8, 59.5	59.50 ± 1.30%	70.5, 72.8, 71.8	71.70 ± 1.15%	70.8, 73.1, 71.8	71.90 ± 1.15%
2.50	66.1, 68.9, 67.5	67.50 ± 1.40%	74.2, 76.9, 75.7	75.60 ± 1.35%	72.4, 74.9, 73.5	73.60 ± 1.25%
5.00	72.5, 75.1, 74.1	73.90 ± 1.31%	80.1, 82.5, 81.3	81.30 ± 1.20%	78.5, 80.9, 79.7	79.70 ± 1.20%
10.00	78.2, 80.8, 79.5	79.50 ± 1.30%	82.1, 84.4, 83.4	83.30 ± 1.15%	82.3, 84.6, 83.6	83.50 ± 1.15%
Taxol (+control)	87.8, 90.5, 89.3	89.20 ± 1.35%	89.8, 92.4, 91.4	91.20 ± 1.31%	89.8, 92.4, 91.4	91.20 ± 1.31%
IC50 (µg/mL)	—	1.10 ± 0.04	—	0.90 ± 0.03	—	0.90 ± 0.03

Table VII. Concentration-dependent cytotoxicity (MTT assay, 24 h; % inhibition, individual biological replicates R1–R3 and mean ± SD, n = 3) of O. esculentum-synthesized Ag/AgCl nanoparticles against MCF-7, HeLa, and HepG2 human cancer cell lines, including the taxol positive-control response and the derived IC50 (mean ± SD) for each cell line.

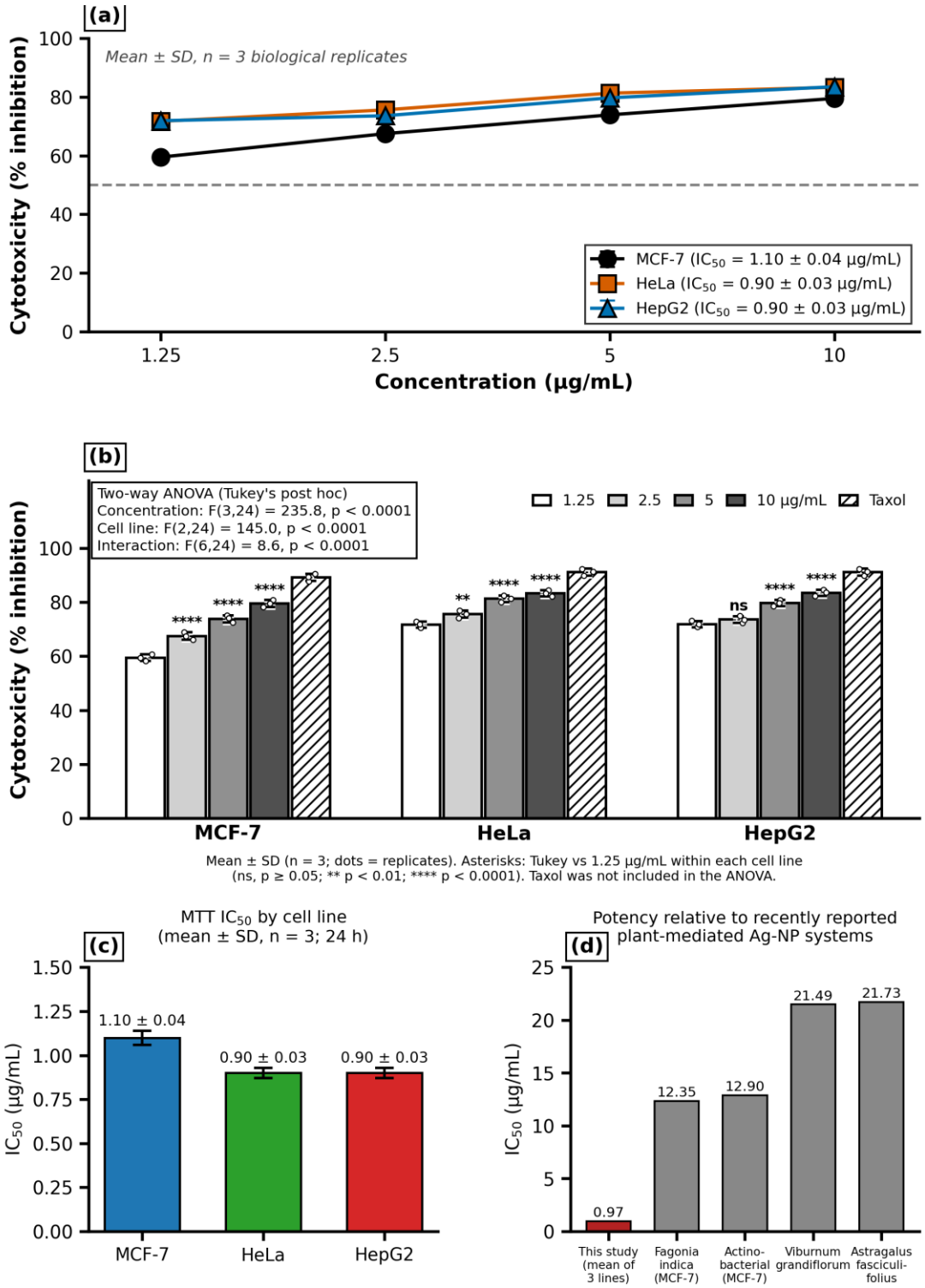


Fig. 9. In vitro antineoplastic activity (MTT assay, 24 h; n = 3 independent biological replicates). (a) Dose–response of MCF-7, HeLa, and HepG2 cells (mean ± SD; dashed line = 50% inhibition). (b) Cytotoxicity across concentrations and cell lines with the taxol positive control; error bars = SD, dots = individual replicates; two-way ANOVA with Tukey's post hoc test (asterisks: significance versus 1.25 µg/mL within each cell line; ns, not significant; ** p < 0.01; **** p < 0.0001). (c) Comparison of IC50 values (mean ± SD) across the three cell lines. (d) Potency (IC50) of O. esculentum Ag/AgCl nanoparticles relative to other recently reported plant-mediated Ag-NP systems tested against comparable cancer cell lines (Ullah et al., 2020; Wypij et al., 2021; Talib et al., 2024; Nosrati et al., 2025).

Two-way ANOVA of the replicate data showed significant main effects of nanoparticle concentration ($F(3,24) = 235.8$, $p < 0.0001$) and cell line ($F(2,24) = 145.0$, $p < 0.0001$), together with a significant concentration × cell-line interaction ($F(6,24) = 8.6$, $p < 0.0001$), indicating that the dose–response differed between cell lines (Fig. 9b). Tukey's post hoc test showed that, relative to 1.25 µg/mL, all higher concentrations produced significantly greater inhibition in MCF-7 cells ($p < 0.0001$) and in HeLa cells (2.5 µg/mL, $p < 0.01$; 5 and 10

µg/mL, $p < 0.0001$), whereas in HepG2 cells the 2.5 µg/mL dose was not significantly different from 1.25 µg/mL (ns) and only 5 and 10 µg/mL were significantly higher ($p < 0.0001$).

Antioxidant (DPPH) activity

Triplicate DPPH assay showed concentration-dependent radical-scavenging activity (one-way ANOVA: $F(4,10) = 399.0$, $p < 0.0001$; Table VIII, Fig. 10). Mean percentage inhibition increased from 43.24 ± 0.18% at 50 µg/mL to 62.66 ± 0.72% at 400 µg/mL, giving a triplicate-derived IC50 of 83.63 ± 1.37 µg/mL (mean ± SD, n = 3; individual replicate IC50s: 84.02, 84.77, and 82.11 µg/mL).

Concentration (µg/mL)	% Inhibition (mean ± SD, n = 3)
50	43.24 ± 0.18
100	51.17 ± 0.95
200	55.32 ± 0.25
300	60.09 ± 0.84
400	62.66 ± 0.72
IC50 (µg/mL)	83.63 ± 1.37 (n = 3)

Table VIII. DPPH radical-scavenging activity of O. esculentum-synthesized Ag/AgCl nanoparticles (mean ± SD, n = 3 independent replicates).

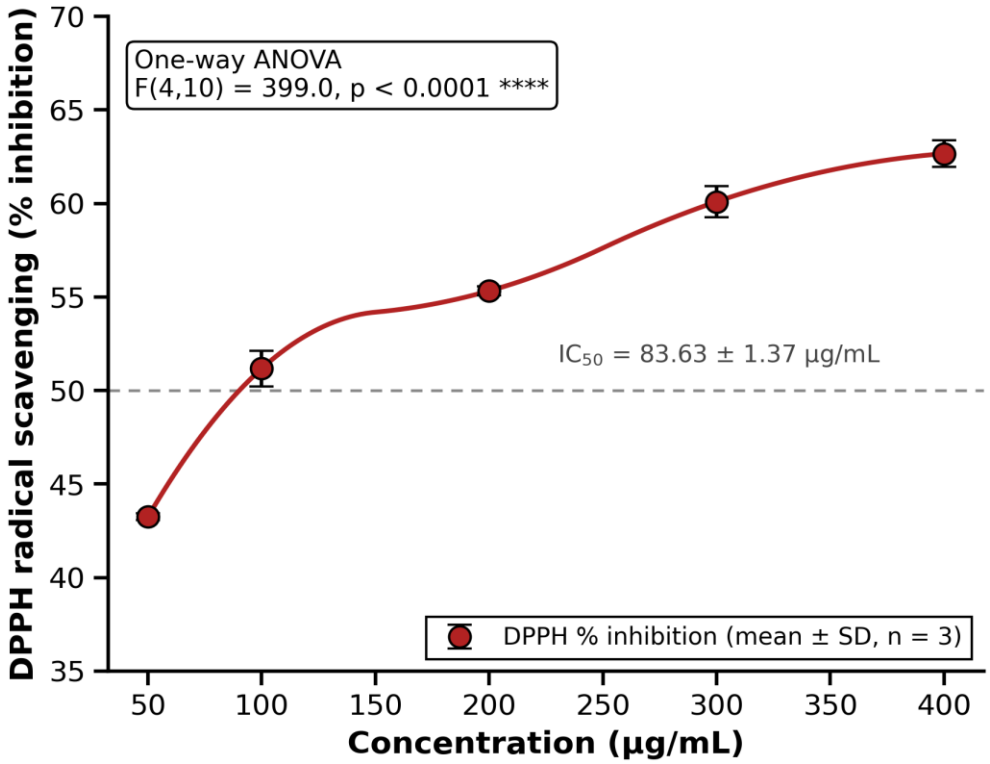


Fig. 10. Triplicate DPPH dose-response curve. Points show mean % inhibition ± SD (n = 3); one-way ANOVA confirms a highly significant dose-response effect (**$p < 0.0001$).**

DISCUSSION

The central finding of this study is the potent, concentration-dependent antineoplastic activity of Oxystelma esculentum-mediated Ag/AgCl nanoparticles against MCF-7, HeLa, and HepG2 cells (Section 3.6). The physicochemical characterization discussed first below — DLS/zeta, optical, crystallographic, morphological, and elemental — is presented specifically to identify the structural basis of that anticancer activity, before the antineoplastic and antioxidant findings themselves are discussed in mechanistic detail.

The DLS-guided screening step showed that hydrodynamic particle size rose steadily with increasing plant-extract concentration across the five formulations (92–113 nm, F1–F5), consistent with extract-mediated agglomeration: at higher phytochemical loading, more extensive bridging/aggregation between nascent nanoparticles competes with, and eventually outweighs, the size-limiting effect of a denser capping layer a concentration-dependent size trend also reported for other plant-extract-mediated Ag-NP systems (Jalab et al., 2021). Selecting the lowest-extract formulation (F1, 92 nm) as the optimum batch for full characterization is therefore a defensible, size-minimizing design choice, and the moderate-stability zeta potential obtained for this formulation (−24.8 mV)

indicates that this size benefit was not purchased at the cost of colloidal instability a prerequisite for the reproducible, batch-to-batch dosing on which the antineoplastic evaluation below depends.

The SPR band at 430 nm observed by UV-Vis spectroscopy is the hallmark optical signature of metallic silver nanoparticles, arising from collective oscillation of conduction electrons at the particle surface (Kelly et al., 2003). The narrow, symmetric band shape is indicative of predominantly spherical, moderately uniform particles, while the weak shoulder near 570–580 nm points to a minor sub-population of larger or lightly aggregated particles consistent with both the DLS secondary population and the size heterogeneity subsequently confirmed by SEM. A single, well-defined SPR band of this kind also served as the batch-release quality-control marker confirming a homogeneous nanoparticle preparation before it was carried forward into the MTT and DPPH assays.

The XRD data indicate a biphasic Ag^0/AgCl nanocrystalline product rather than phase-pure metallic silver. This is a common and well-documented outcome of green, plant-extract-mediated synthesis, in which residual chloride ions in the extract precipitate a fraction of the unreduced Ag^+ as AgCl while the remainder is reduced to Ag^0 by phytochemical reducing agents — a biphasic Ag^0/AgCl product has recently been reported from other plant- and biowaste-mediated green syntheses (e.g., Jatropha seed extract; Abdel-Hafeez and Abdel-Goad, 2025). Ag/AgCl heterostructures are themselves of interest as plasmonic photocatalysts, and naked Ag/AgCl nanoparticles have been reported to show intrinsic photocatalytic anticancer activity in their own right (Zhang et al., 2022), so this finding is reported explicitly as "Ag/AgCl nanoparticles" throughout this manuscript rather than described simply as "Ag-NPs," to remain consistent with the XRD evidence.

The SEM-derived particle size (pooled mean 74.3 nm; primary-particle estimate 50.7 nm) exceeded the XRD-derived crystallite size (≈20–30 nm), indicating that the SEM-visible particles are polycrystalline agglomerates composed of multiple smaller Ag^0/AgCl crystallites rather than single crystals a relationship also consistent with the larger hydrodynamic size measured by DLS (92 nm for the same formulation), since DLS reports the diffusing hydrodynamic radius of the (often lightly solvated/agglomerated) particle in suspension, which is expected to exceed both the dry-state SEM projected diameter and the XRD coherent-domain size — a size hierarchy (DLS ≥ SEM/TEM > XRD) previously documented for other agglomerated Ag-NP systems (Sharma et al., 2020). This is further supported by EDX, where the distinct Cl signal (5.38 ± 0.42 wt%, mean of four spectra) alongside Ag (10.90 ± 0.51 wt%) independently corroborates the AgCl phase identified by XRD at a consistent Ag:Cl atomic ratio (0.67 ± 0.02), and the dominance of C, N, and O (collectively ≈ 74 wt%) is consistent with the organic, biomolecule-derived capping layer identified in detail by FTIR (O–H/N–H, C=C/amide, C–N/carboxylate, C–O, and Ag–O vibrations). Notably, the 50–74 nm SEM size range obtained here falls within the window reported to support efficient cellular internalization of Ag-NPs in mammalian cells (Wu et al., 2019), which is directly relevant to interpreting the antineoplastic activity discussed below.

Against all three cancer cell lines, the Ag/AgCl nanoparticles' cytotoxic activity at the highest tested concentration reached 89–92% of the taxol positive-control response, and the mean IC50 across the three lines (0.97 µg/mL; individual IC50 values 1.10 ± 0.04, 0.90 ± 0.03, and 0.90 ± 0.03 µg/mL, n = 3) is markedly lower (more potent) than several recently reported plant-mediated Ag-NP systems evaluated against comparable cell lines: Fagonia indica Ag-NPs against MCF-7 (IC50 = 12.35 µg/mL; Ullah et al., 2020), protein-capped (actinobacterial) Ag-NPs against MCF-7 (IC50 = 12.9 µg/mL; Wypij et al., 2021), methanolic Viburnum grandiflorum Ag-NPs against a rhabdomyosarcoma cell line (IC50 = 21.49 µg/mL; Talib et al., 2024), and root-extract Astragalus fasciculifolius Ag-NPs against MCF-7 (IC50 = 21.73 µg/mL; Nosrati et al., 2025). Direct comparison should nonetheless be made cautiously given differences in exposure time, cell passage, and assay conditions across studies, and the possibility that the AgCl component itself contributes to the observed cytotoxicity (via slow Ag^+ release) rather than the effect being attributable to metallic Ag^0 alone a distinction the present single-batch design cannot resolve and that merits dedicated follow-up (e.g., comparison against phase-pure Ag^0 and phase-pure AgCl controls).

Because the MTT assay was performed in three independent biological replicates, the dose–response relationship could be tested formally: two-way ANOVA indicated significant concentration and cell-line effects and a significant interaction (all $p < 0.0001$), and Tukey's post hoc test showed that the dose–response profile differed between lines — a progressive, significant increase across the tested range in MCF-7 cells, but a plateau between 1.25 and 2.5 µg/mL in HepG2 cells (ns). Because even the lowest tested concentration (1.25 µg/mL) produced more than 50% inhibition in all three cell lines, the reported IC50 values lie below the lowest tested concentration; including lower concentrations (e.g., 0.1–1 µg/mL) in future assays would allow the IC50 to be interpolated more precisely.

By contrast, DPPH radical-scavenging activity was moderate (IC50 = 83.63 ± 1.37 µg/mL) roughly two orders of magnitude higher than the cytotoxic IC50 values. At the concentrations effective against cancer cells (0.9–1.1 µg/mL), the Ag/AgCl nanoparticles are therefore unlikely to be meaningfully scavenging free radicals by extrapolation from the DPPH dose-response curve, whereas at the much higher concentrations used in the cell-free DPPH assay, the phytochemical capping layer is sufficiently concentrated to act as a direct chemical radical scavenger in vitro. This wide, roughly two-order-of-magnitude separation between the cytotoxic and antioxidant concentration ranges is a notable and potentially favourable feature for a candidate anticancer agent: it suggests that at anticipated therapeutic (cytotoxic) doses, these nanoparticles would act predominantly through pro-oxidant, apoptosis-inducing mechanisms in target cancer cells, a mode of action documented for Ag-NPs specifically in HepG2 cells via ROS-mediated MAPK/AKT/p53 signalling and caspase-3 activation (Zhu et al., 2016), in MCF-7 cells via ROS-dependent caspase-3/9 activation (Ullah et al., 2020), and more broadly across cancer cell types via ROS-dependent pro-apoptotic signalling (Yuan et al., 2022) rather than through competing antioxidant activity

that might otherwise blunt their own cytotoxic efficacy. As no ROS or apoptotic markers were directly measured in the present study, this mechanistic interpretation remains a hypothesis for dedicated follow-up (e.g., DCFDA-based ROS quantification, caspase activity assays, Annexin V/PI staining) rather than a demonstrated finding.
Taken together, the coherence across DLS/zeta, UV-Vis, XRD, SEM/EDX, and FTIR data all independently pointing to a moderately stable, biomolecule-capped, biphasic Ag^0/AgCl nanocrystalline product together with its markedly potent anticancer activity relative to recently published comparators, supports the pharmacological promise of Oxystelma esculentum-mediated Ag/AgCl nanoparticles, while the biphasic AgCl component additionally suggests potential relevance to plasmonic photocatalytic applications beyond the biomedical scope of this study.

CONCLUSION

This study establishes Oxystelma esculentum-mediated Ag/AgCl nanoparticles as potent antineoplastic agents against MCF-7, HeLa, and HepG2 cancer cell lines (IC50 = 0.90–1.10 µg/mL), substantially outperforming several recently reported plant-mediated Ag-NP systems. This activity was underpinned by a five-formulation, DLS-guided screening strategy that identified an optimum batch (92 nm hydrodynamic size, −24.8 mV zeta potential), comprehensively characterized by UV-Vis spectroscopy, XRD (Scherrer and Williamson–Hall analysis), SEM (automated particle-size distribution, n = 2,203 particles), EDX (four-spectrum mean composition), and FTIR, confirming the formation of a biomolecule-capped, biphasic Ag^0/AgCl nanocrystalline product with a mean particle size in the 50–74 nm range (SEM) and 27–29 nm crystallite size (XRD) — a structural profile consistent with efficient cellular uptake and with the AgCl phase's own reported contribution to cytotoxicity. The nanoparticles additionally showed statistically significant, moderate DPPH radical-scavenging activity (IC50 = 83.63 ± 1.37 µg/mL) as a secondary readout. These findings support the potential of O. esculentum-mediated Ag/AgCl nanoparticles as candidate anticancer agents warranting further mechanistic (ROS/apoptosis pathway) and in vivo investigation, alongside replicate (triplicate) MTT testing to permit formal statistical comparison across cell lines.

ACKNOWLEDGMENTS

Not applicable.

FUNDING

There was no funding.

DATA AVAILABILITY STATEMENT

The datasets generated and/or analysed during the current study are available from the corresponding author on reasonable request.

ETHICAL APPROVAL

Not applicable.

CONSENT TO PUBLICATION

The authors confirm that this manuscript is original, has not been published previously in any language or format, and is not currently under review elsewhere.

LIST OF ABBREVIATIONS

Ag-NPs — Silver nanoparticles
ANOVA — Analysis of variance
DLS — Dynamic light scattering
DPPH — 2,2-Diphenyl-1-picrylhydrazyl
ECD — Equivalent circular diameter
EDX — Energy-dispersive X-ray spectroscopy
fcc — Face-centred cubic
FTIR — Fourier-transform infrared spectroscopy
FWHM — Full width at half maximum
IC50 — Half-maximal inhibitory concentration
JCPDS — Joint Committee on Powder Diffraction Standards
MTT — 3-(4,5-Dimethylthiazol-2-yl)-2,5-diphenyltetrazolium bromide
ROS — Reactive oxygen species
SD — Standard deviation
SEM — Scanning electron microscopy
SPR — Surface plasmon resonance
UV-Vis — Ultraviolet-visible spectroscopy
W–H — Williamson–Hall
XRD — X-ray diffraction

CONFLICT OF INTEREST

The authors declare no conflict of interest.

REFERENCES

1. Abdel-Hafeez AM and Abdel-Goad MAH (2025). Green synthesis of Ag/AgCl nanoparticles using Jatropha seed extract for photocatalytic degradation and antibacterial treatment of petroleum industry wastewater. Discov. Sustain., 6: 906. DOI: 10.1007/s43621-025-01139-3
2. Ahmed S, Ahmad M, Swami BL and Ikram S (2016). A review on plants extract mediated synthesis of silver nanoparticles for antimicrobial applications: A green expertise. J. Adv. Res., 7(1): 17-28. DOI: 10.1016/j.jare.2015.02.007
3. Bhattacharjee S (2016). DLS and zeta potential – what they are and what they are not? J. Control. Release, 235: 337-351. DOI: 10.1016/j.jconrel.2016.06.017
4. Blois MS (1958). Antioxidant determinations by the use of a stable free radical. Nature, 181: 1199-1200. DOI: 10.1038/1811199a0
5. Jalab J, Abdelwahed W, Kitaz A and Al-Kayali R (2021). Green synthesis of silver nanoparticles using aqueous extract of Acacia cyanophylla and its antibacterial activity. Heliyon, 7(9): e08033. DOI: 10.1016/j.heliyon.2021.e08033
6. Kelly KL, Coronado E, Zhao LL and Schatz GC (2003). The optical properties of metal nanoparticles: The influence of size, shape, and dielectric environment. J. Phys. Chem. B, 107(3): 668-677. DOI: 10.1021/jp026731y
7. Khan I, Saeed K and Khan I (2019). Nanoparticles: Properties, applications and toxicities. Arab. J. Chem., 12(7): 908-931. DOI: 10.1016/j.arabjc.2017.05.011
8. Maqbool, M. S., Abbas, R. Z., Tahir, S., Tariq, N., Razakova, R., Babaevna, S. S., & Rajabov, T. (2026). Green-synthesized gold nanoparticles: as emerging tools to combat antimicrobial resistance and therapeutic applications in poultry. *Veterinary Research Communications*, *50*(3), 215. https://doi.org/10.1007/s11259-026-11150-2
9. Mosmann T (1983). Rapid colorimetric assay for cellular growth and survival: application to proliferation and cytotoxicity assays. J. Immunol. Methods, 65(1-2): 55-63. DOI: 10.1016/0022-1759(83)90303-4
10. Nosrati F, Fakheri B, Ghaznavi H, Mahdinezhad N, Sheervalilou R and Fazeli-Nasab B (2025). Green synthesis of silver nanoparticles from plant Astragalus fasciculifolius Bioss and evaluating cytotoxic effects on MCF7 human breast cancer cells. Sci. Rep., 15: 25474. DOI: 10.1038/s41598-025-05224-5
11. Scherrer P (1918). Bestimmung der Größe und der inneren Struktur von Kolloidteilchen mittels Röntgenstrahlen. Nachr. Ges. Wiss. Göttingen, 26: 98-100. (Pre-DOI-era publication; no DOI assigned.)
12. Sharma V, Verma D and Okram GS (2020). Influence of surfactant, particle size and dispersion medium on surface plasmon resonance of silver nanoparticles. J. Phys.: Condens. Matter, 32(14): 145302. DOI: 10.1088/1361-648X/ab601a
13. Talib H, Mehmood A, Amjad MS, Mustafa A, Khan MAR, Raffi M, Khan RT, Ahmad KS and Qureshi H (2024). Antibacterial, antioxidant, and anticancer potential of green fabricated silver nanoparticles made from Viburnum grandiflorum leaf extract. Bot. Stud., 65: 4. DOI: 10.1186/s40529-024-00411-5
14. Ullah I, Khalil AT, Ali M, Iqbal J, Ali W, Alarifi S and Shinwari ZK (2020). Green-synthesized silver nanoparticles induced apoptotic cell death in MCF-7 breast cancer cells by generating reactive oxygen species and activating caspase 3 and 9 enzyme activities. Oxid. Med. Cell. Longev., 2020: 1215395. DOI: 10.1155/2020/1215395
15. Williamson GK and Hall WH (1953). X-ray line broadening from filed aluminium and wolfram. Acta Metall., 1(1): 22-31. (Pre-DOI-era publication; no DOI assigned.)
16. Wu M, Guo H, Liu L, Liu Y and Xie L (2019). Size-dependent cellular uptake and localization profiles of silver nanoparticles. Int. J. Nanomedicine, 14: 4247-4259. DOI: 10.2147/IJN.S201107
17. Wypij M, Jędrzejewski T, Trzcińska-Wencel J, Ostrowski M, Rai M and Golińska P (2021). Green synthesized silver nanoparticles: Antibacterial and anticancer activities, biocompatibility, and analyses of surface-attached proteins. Front. Microbiol., 12: 632505. DOI: 10.3389/fmicb.2021.632505
18. Yuan J, Khan SU, Luo J, Jiang Y, Yang Y, Yan J and Tong Q (2022). Biosynthetic silver nanoparticles inhibit the malignant behavior of gastric cancer cells and enhance the therapeutic effect of 5-fluorouracil by promoting intracellular ROS generation and apoptosis. Pharmaceutics, 14(10): 2109. DOI: 10.3390/pharmaceutics14102109
19. Zhang X, Wu J, Xu J, Liu D, Chen R and Xu Z, et al. (2022). Photocatalytic anticancer performance of naked Ag/AgCl nanoparticles. Chem. Eng. J., 428: 131265. DOI: 10.1016/j.cej.2021.131265
20. Zhang X-F, Liu Z-G, Shen W and Gurunathan S (2016). Silver nanoparticles: Synthesis, characterization, properties, applications, and therapeutic approaches. Int. J. Mol. Sci., 17(9): 1534. DOI: 10.3390/ijms17091534
21. Zhu B, Li Y, Lin Z, Zhao M, Xu T, Wang C and Deng N (2016). Silver nanoparticles induce HePG-2 cells apoptosis through ROS-mediated signaling pathways. Nanoscale Res. Lett., 11: 198. DOI: 10.1186/s11671-016-1419-4